

# Multichannel driving triboelectric nanogenerator for enhancing the output charge density

Ruichao Zhang, Mingmin Hao, Suo Bai, Peizu Song, Xiaofeng Jia, Weihao Gao, Qi Xu, Juan Wen, Li Cheng<sup>\*</sup>, Yong Qin<sup>\*</sup>

*Institute of Nanoscience and Nanotechnology, School of Materials and Energy, Lanzhou University, Lanzhou 730000, China*

## ARTICLE INFO

### Keywords:

Triboelectric nanogenerator  
Multichannel driving  
External electric field  
Inner electric field  
High charge density

## ABSTRACT

The output charge density is recognized as the most important parameter to characterize the performance of triboelectric nanogenerators (TENGs). In this paper, we report a multichannel driving TENG (MTNG) through utilizing the external electric field outside the friction layers pair ( $E_{\text{ext}}$ ) to drive the flow of electrons in multiple channels and generate multiple outputs simultaneously, which is different from the past TENGs that drive them flowing in a single channel. Through increasing the number of driving channels and decreasing the thickness of dielectric layers in the driving channels, the output charge density of MTNG is increased to  $5.35 \text{ mC m}^{-2}$ , which is the highest reported value of TENGs by now. This work provides a new path to increase the output performance of TENGs.

## 1. Introduction

The continuous developments in triboelectric nanogenerators (TENGs) have demonstrated their substantial potential as a high-efficiency, low-cost and easy fabrication mechanical energy harvesting technology [1–4]. In particular, it provides a long-life and environmentally friendly power source for small-size electronic devices in different scenarios such as portable electronic devices, implantable devices and wireless monitoring system [5–12]. Since the invention of TENG in 2012 [13], a series of efforts have been made to improve its output performance including the output voltage, current, power and charge density [14–19]. Among them, the output charge density is gradually recognized as a key important parameter to evaluate the performance of TENGs for the following reasons. First, the output voltage and current of TENGs vary with the changes of the driving force, but the output charge density remains basically constant under different driving force and reflects the intrinsic performance of TENG itself. Hence, the output charge density could accurately assess the performance of TENGs. Second, in practical applications, as the load resistances are usually much lower than the optimum load resistance of the TENGs, most of the generated energy is consumed by the inner resistance of the TENGs. Under this circumstance, the actual power acted on the loads mainly depends on the output current of a TENG, which mainly depends on its charge density and driving frequency.

Since the driving frequency is determined by the environmental vibrations, the output current especially the average current is intrinsically determined by the charge density. Therefore, the output charge density can reflect the TENG's ability of exporting energy to the loads.

In order to increase the output charge density of TENG, many technique ways have been explored and developed, which could be divided into two categories. The first one is to increase the essential performance of TENG itself through materials selection, structure optimization, charge injection and so on [20–26]. It is essentially to increase the charge density of the friction layers pair. By exploring these methods, a TENG with a multigap-structured friction layer exhibits a maximum output charge density of  $2.94 \text{ mC m}^{-2}$  [27]. Besides the above methods to enhance the essential performance of the TENG, a series of intensifier circuits including charge pumping circuits and step-down circuits are developed as the second category of methods to increase the TENG's output charge density to the external circuits under circumstance of limited essential output performance of TENG itself [28–33]. For the TENG with the charge pump circuit, a maximum output charge density of  $4.76 \text{ mC m}^{-2}$  is obtained [34]. At present, although the output charge density of TENGs has been increased to a fairly high value, it is still not enough for the killer applications of TENGs and is the key challenge in this field. Further increasing the output charge density is of key point for the development and applications of TENGs.

For the past TENGs, there are three characteristics: 1. Changes of the

<sup>\*</sup> Corresponding authors.

*E-mail addresses:* [chengl2007@live.cn](mailto:chengl2007@live.cn) (L. Cheng), [qinyong@lzu.edu.cn](mailto:qinyong@lzu.edu.cn) (Y. Qin).

<https://doi.org/10.1016/j.nanoen.2022.107272>

Received 4 February 2022; Received in revised form 7 April 2022; Accepted 8 April 2022

Available online 12 April 2022

2211-2855/© 2022 Published by Elsevier Ltd.

inner electric field between the friction layers pair ( $E_{in}$ ) is used to generate the induced potential in electrodes pair which drives the moving of electrons in external circuit; 2. An electrodes pair surrounding the friction layers pair is the only way to use the  $E_{in}$  since the friction layers contact with each other in some stage of a TENG's working cycle. 3. As the electrodes pair shields the electric field outside it, it is impossible to add another electrodes pair outside the existed one to increase the output charge density. These characteristics determine, for the designs used in past TENGs, their friction layers pair's charge density is the extremum of their output charge density. However, besides  $E_{in}$ , there also exists an external electric field outside the friction layers pair ( $E_{ext}$ ).  $E_{ext}$  has the following characteristics: 1.  $E_{ext}$  also changes with the moving of friction layers pair to generate the induced potential in electrodes pair and drive electrons moving. That is to say, it could also be used to generate electricity; 2. As the space of  $E_{ext}$  is open, many electrodes pairs could be set in  $E_{ext}$  at the same time; 3. The electrodes pair in  $E_{ext}$  only shields the electric field in the electrodes pair. In the space outside the electrodes pair,  $E_{ext}$  still exists. Thus, multiple electrodes pairs existing in  $E_{ext}$  could simultaneously generate electricity. So, if  $E_{ext}$  is used, it is possible to fabricate a new kind of TENG with multiple driving channels, and its total output charge density could be increased well above the friction layers pair's charge density.

In this work, we developed a multichannel driving triboelectric nanogenerator (MTNG) through utilizing  $E_{ext}$  to present a new way to further increase the output charge density of TENGs. The total output charge density of a MTNG is many times that of a normal TENG (N-TENG) also working in the contact-separate mode with the same friction layers pair. The highest total output charge density of MTNG reaches  $5.35 \text{ mC m}^{-2}$ , which is about 20 times that of N-TENG, 1.82 times of the highest reported value of TENG's essential output charge density and even  $0.59 \text{ mC m}^{-2}$  higher than the highest reported value of TENGs with

the help of intensifier circuits. MTNG can also effectively avoid crosstalk noise between multiple devices driven at the same time and improve their working efficiency. Furthermore, through collecting the output energy in capacitors, a rather high energy consuming device could be driven.

## 2. Results and discussion

### 2.1. Design of the MTNG

Fig. 1a shows the calculated result of the electric field generated by the friction layers pair, the electric field in the whole space can be split into two parts:  $E_{in}$  and  $E_{ext}$ . Compared with  $E_{in}$ ,  $E_{ext}$  exists in a much larger space. At the same time, considering that the electrodes pair in  $E_{ext}$  will not shield the electric field outside itself, in the space outside this electrodes pair,  $E_{ext}$  still exists. So, it is possible to set a mass of electrodes pairs in it to realize multichannel driving in a TENG. However, to utilize the multiple electrodes pairs setting in  $E_{ext}$  to effectively generate electricity, there are still two requirements to be met: 1. The electrodes pairs should work simultaneously; 2. Because the intensity of  $E_{ext}$  is much lower than that of  $E_{in}$ , new design should be developed to increase  $E_{ext}$ 's intensity to get higher output charge density from each electrodes pair.

For the first requirement, as Fig. 1b I-III show, if a short-connected electrodes pair is put in the electric field (intensity is  $E$ ), positive and negative charges will respectively move to the two electrodes and shield the electric field between the electrodes. The charge density on the electrodes ( $\delta_e$ ) could be calculated with the following equation [35]:

$$\delta_e = \epsilon_0 \epsilon_r E$$

In this equation,  $\epsilon_0$  is the permittivity of the vacuum and  $\epsilon_r$  is the

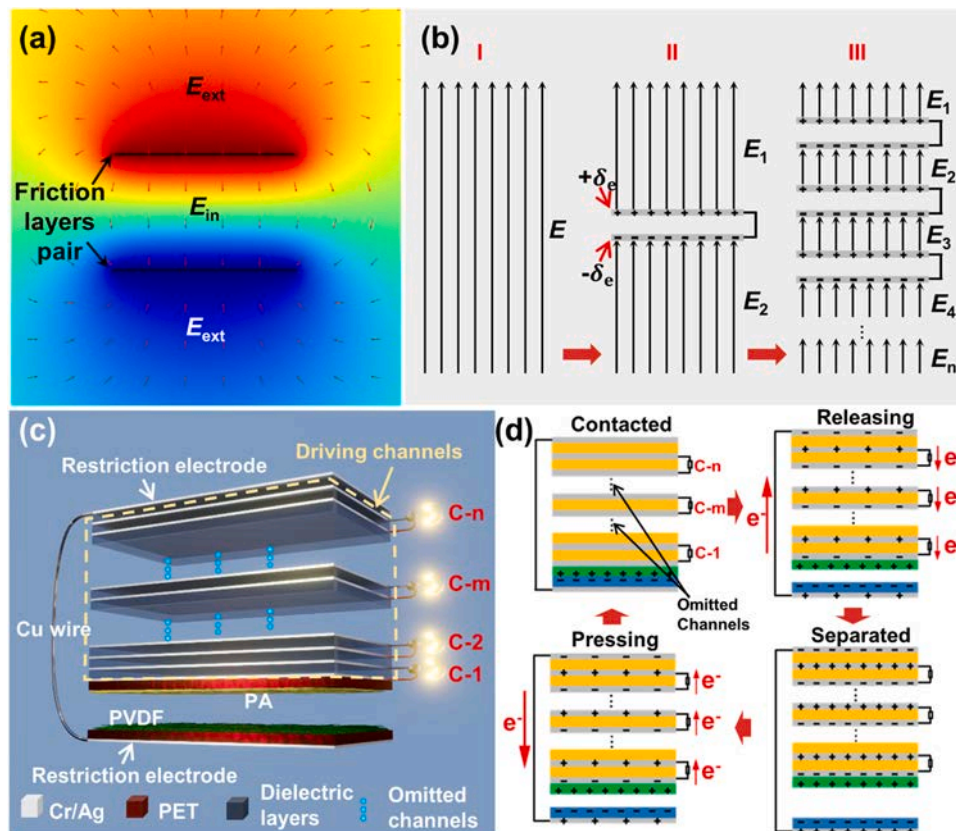


Fig. 1. Design of the MTNG. (a) Simulated result of the potential and electric field intensity distribution generated by the friction layers pair. (b) Changes of the electric field and distributions of charges after put one or more short-connected electrode pairs in the electric field. (c) Schematic illustration of the MTNG. (d) Moving behavior of charges in the circuit in the working process of the MTNG.

permittivity of the medium. As a result, the electric field is divided into two parts (intensities are  $E_1$  and  $E_2$ ), if the boundary effect is ignored, the intensities fit the equation:  $E_1 = E_2 = E$ . That is to say, the added electrodes pair influences little to the electric field out of it. So, if multiple electrodes pairs are set in the electric field, the inductive charges existed on all of them. Therefore, the many pairs of electrodes pair parallel with each other could work simultaneously in  $E_{ext}$ .

For the second requirement, an electric field restriction mechanism is introduced to improve the electric field intensity. As Fig. S1 shows, a pair of restriction electrodes is short circuit connected and added in  $E_{ext}$ . One electrode at the back of bottom frictional layer and the other electrode is set above the top frictional layer with a gap between them. Statistical results in Fig. S1a and b show, after adding the restriction electrodes,  $E_{ext}$  is restricted in the gap and its intensity is remarkably increased, the value along the arrows is about 5 times that of without restriction electrodes (Fig. S1c).

Fig. 1c shows the structure of MTNG, electrospinning polyvinylidene fluoride (PVDF) and polyamides (PA) nanofibers film (scanning electron microscopy (SEM) images shown in Fig. S2a-b, Fig. S3 shows their surface potentials after rubbing are about  $-2210$  V and  $1580$  V, respectively) are used as the friction layers pair, a series of electrodes pairs with dielectric layers between them (sectional SEM image shown in Fig. S2c) are placed at the top of the PA friction layer as driving channels, the restriction electrodes are placed at the top of the driving

channels and at the bottom of the PVDF friction layer and connected by a copper wire. So, in the MTNG, all driving channels are placed in the restricted  $E_{ext}$ . (Fabrication process of the MTNG is given in the Material and methods.)

Fig. 1d shows the transfer behavior of charges in the circuit. When the friction layers pair is brought into physical contact, a lot of triboelectric charges will generate on the two friction layers surfaces. Then, when the MTNG at the contact state, the friction layers pair contacted, which will not generate electric field in the space, and no charge will be induced in the driving channels. And when MTNG is releasing, the friction layers pair will generate electric field in the space, and the  $E_{ext}$  induced charges in the electrodes of the driving channels, and driving charges moving in the circuit along the marked direction. At the separated state,  $E_{ext}$  reaches it maximum value, and the induced maximum charges is obtained in the driving channels. Then, when the MTNG is pressing, intensity of  $E_{ext}$  decreasing, and charges move back in the circuit. Thus, when the MTNG is pressing or releasing, the charges will transfer through the external circuit connected to each driving channel. So, in the working cycle of the MTNG, charges move alternately in the circuits to generate electricity in external circuits.

### 2.2. Output performance of MTNG with 3 driving channels

A MTNG with 3 driving channels (MTNG-3) was designed and

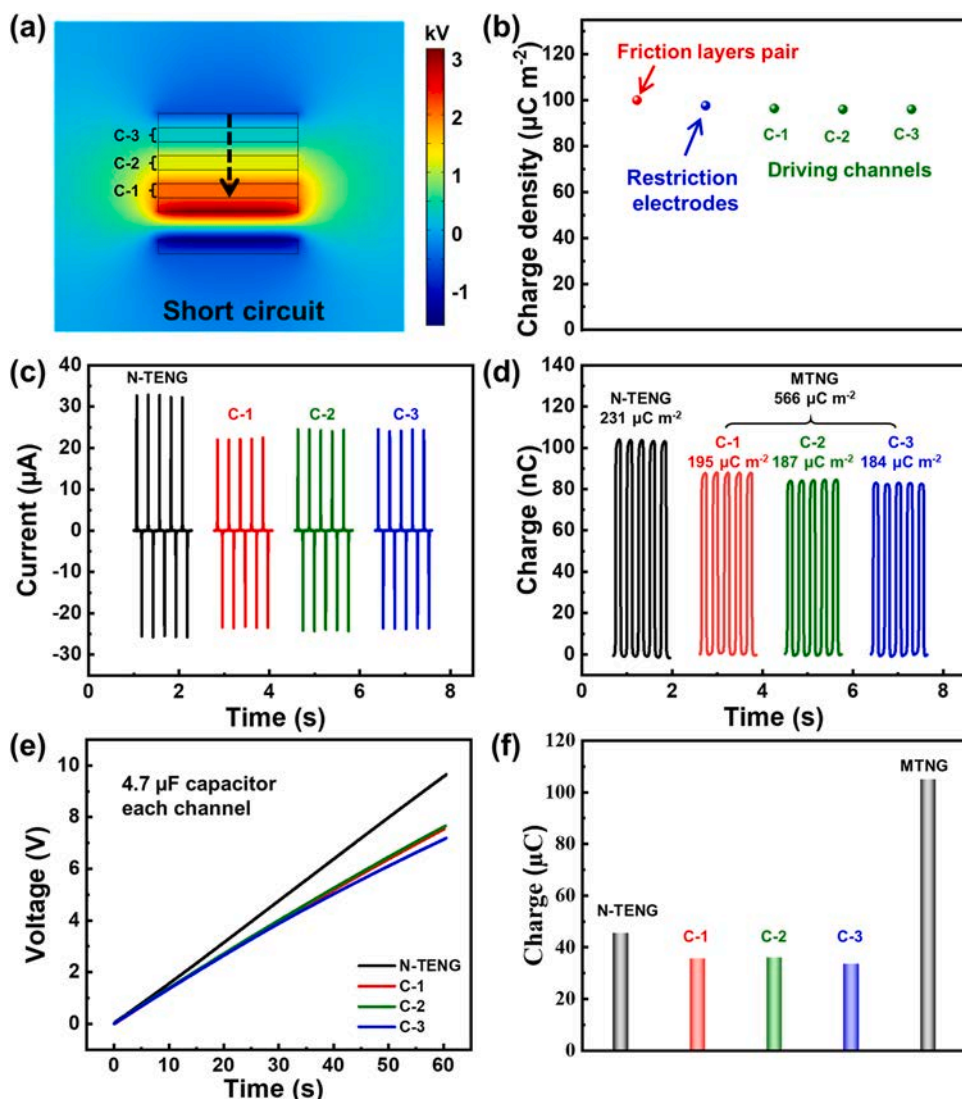


Fig. 2. Performance of an MTNG-3. (a) Simulated result of the potential distribution in the MTNG-3 at the condition of driving channels short circuit connected. (b) Simulated results of the charge density on the friction layers pair, the restriction electrodes and the driving channels of the MTNG-3 at the condition of driving channels short circuit connected. (c) and (d) show the output currents and charges of the N-TENG and the driving channels of the MTNG-3. (e) and (f) show the voltage of  $4.7 \mu\text{F}$  capacitors charged by the N-TENG and the driving channels of the MTNG-3 and the calculated result of the charges stored in the capacitors.

fabricated to check the working mechanism and characterize the performance of the MTNG. Fig. 2a, Fig. S4 and S5 show the simulated result of the potential distribution in MTNG-3. When the driving channels are open circuit connected, the potential decreases linearly in the driving channels along the direction away from the friction layer and the electric field is almost uniform. And when the driving channels are short circuit connected, two electrodes of each driving channel have equal potential and the electric field intensity in each driving channel is zero, which indicates that all driving channels shield the electric field inside simultaneously. In other words, the charges move along same direction in all driving channels simultaneously. This result indicates, all driving channels could work in the meantime. As Fig. 2b shows, the calculated charge densities of the driving channels are very close to that of the restriction electrodes, and a little less than that of the friction layers pair. This result implies that output charge density of each driving channel is close to the charge density of the friction layers pair.

Fig. 2c-d and Fig. S6 show the output performance of a MTNG-3 (optical image of the MTNG-3 is shown in Fig. S7). We can see, though output current, voltage and output charge density of one channel of the MTNG is lower than that of the N-TENG (structure of the N-TENG is shown in Fig. S8), total output current and output charge density increases to approximately 2.5 times of the N-TENG. The V-Q plots [36] of the MTNG-3 (shown in Fig. S9) with different load resistances show, when the load resistances are lower than 10 M $\Omega$ , MTNG's output energy is higher than that of the N-TENG. As the resistances of most devices powered by TENGs are not very high, for most applications, MTNG could provide more energy than the N-TENG. Fig. 2e shows the voltage of capacitors charging with MTNG-3 and N-TENG. In 1 min, three 4.7  $\mu$ F capacitors charged simultaneously by the MTNG are respectively reach 7.5 V, 7.6 V and 7.2 V, the total charge quantity (statistical result shown in Fig. 2f) and energy of the capacitors charged by the MTNG-3 are 2.3 times and 1.8 times that of the N-TENG. This result further proves that all the driving channels of the MTNG could work simultaneously to supply more energy to the circuit. As shown in Fig. S10, the stability of

MTNG is also excellent. After continuously working for about 58,000 working cycles, there is no attenuation in the output currents of the driving channels, and the output currents even increase slightly, which caused by the increase of friction charge after long-time work. Furthermore, as the stability of the MTNG mostly depends on the stability of the friction layers pair, the MTNG has the same stability with the N-TENG, which could be proved by the phenomenon that the increase rates of the driving channels and the N-TENG are almost the same.

### 2.3. Further increment of MTNG's output charge density

From the above results, the performance of MTNG-3 is significantly improved compared with the N-TENG. Next, we will explore if there is still enormous potential to further improve its performance. According to the working mechanism of MTNG, there is an apparent method to further increasing the total output current and output charge density of the MTNG through increase the number of driving channels as each driving channel could generate almost the same amount of charge.

Therefore, we fabricated MTNGs with more driving channels. Fig. 3a-c and Fig. S11 show the output of a MTNG with 10 driving channels (MTNG-10). It can be observed that the output current and output charge density of each driving channels are a little less than that of the N-TENG, which is similar to the phenomenon of MTNG-3. The average output current (20.9  $\mu$ A) and average output charge density (186  $\mu$ C m $^{-2}$ ) of each channel of MTNG-10 are respectively 65.7% and 70.7% that of the N-TENG (31.8  $\mu$ A and 263  $\mu$ C m $^{-2}$ ). From the statistical results shown in Fig. 3c, the total output charge density of the MTNG-10 is increased to 1.86 mC m $^{-2}$ , which is about 7.1 times that of N-TENG. Through further increasing the number of driving channels, the total output charge density of MTNG could be further increased. As shown in Fig. 3d, Fig. S12 and S13, for an MTNG with 20 driving channels (MTNG-20), the total output charge density is increased to 2.50 mC m $^{-2}$ , and for an MTNG with 30 driving channels (MTNG-30),

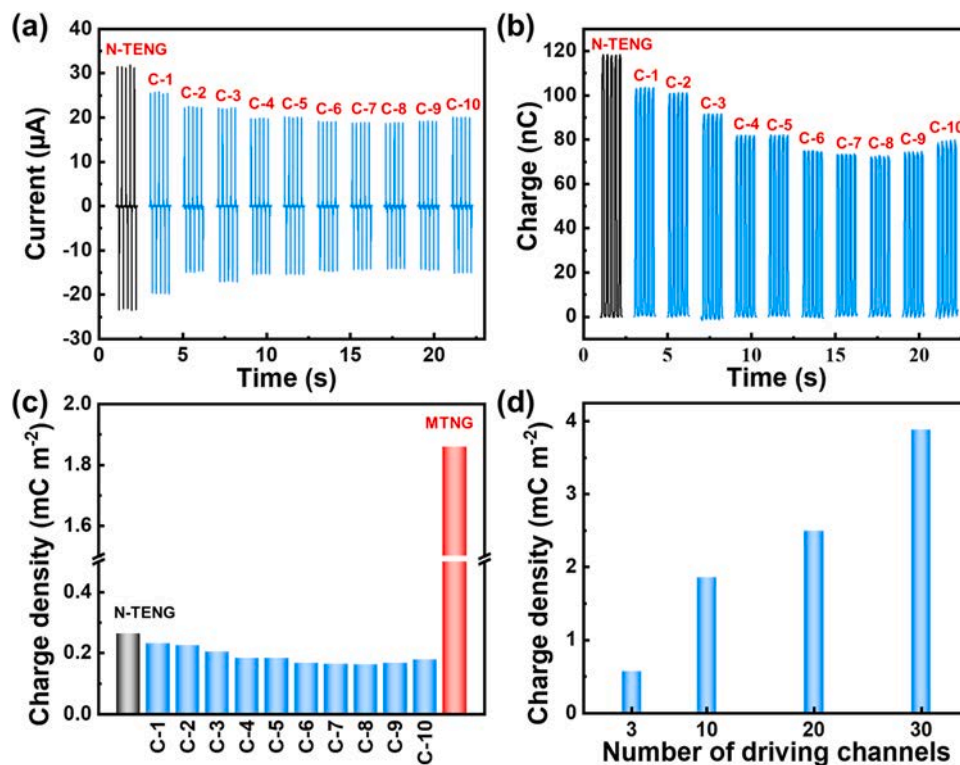


Fig. 3. Incrementation of the performance of MTNG through increase the number of driving channels. (a) and (b) respectively show the output currents and charges of the N-TENG and the driving channels of the MTNG-10. (c) Statistical result of the output charge densities of the N-TENG and the MTNG-10. (d) A bar graph shows the relationship of the output charge densities ranges with the number of driving channels in the MTNG.

the total output charge density is increased to  $3.88 \text{ mC m}^{-2}$ . As shown in simulated result (Fig. S14), output charge density of the MTNG increase rapidly with the number of driving channels in the range of 30–180. These results indicate that adding the external output channels of MTNG is an effective way to improve its performance.

Comparing with the MTNG-3, two differences could be found for MTNGs with more driving channels, the output current and output charge density of the channels at the top and bottom sides of the device are obviously higher than that at the middle of the channels, and the average output of the channels decreases with the increase of its quantity. These changes are caused by the boundary effect which existed widely in the electric field generated by two parallel charged layers. The boundary effect could be briefly described as follows: As well known, two infinite parallel layers with opposite charge will generate a uniform electric field in the space between them. But if the layers are finite, at the boundary of the layers, the electric field lines curve outward, which leads to the decrease of the electric field's intensity especially at the boundary of the layers. Theoretically, if the layers are placed in materials with uniform dielectric constant, the degree of the boundary effect mainly depends on the ratio of the layers' width and the layers' distance. For charged layers with the same width, the degree of the boundary effect increases with the layers' distance, which is exhibited clearly by the simulated result shown in Fig. 4a and b. Comparing with that generated by the layers with smaller distance (marked as II), the electric field generated by the layer with larger distance (marked as I) decreases both at the boundary and the center of the layers. As the charge density of the driving channels depends on the intensity of the electric field surrounding them, the boundary effect leads to the decrement of the driving channels' output charge density.

Consequently, decreasing the boundary effect is another way to increase MTNG's performance, which could be realized by decreasing the thickness of dielectric layers. Fig. 4c shows the simulated result of the charge densities of the driving channels of MTNG-30 s with different dielectric layers' thickness. It can be obviously observed that the charge densities of the driving channels with thinner dielectric layers are higher, especially for the channels in the middle of the device. The above

results indicate that, decreasing the thickness of dielectric layers could increase the MTNG's output charge density.

Since the dielectric constant of the dielectric layers is different from the air surrounding the MTNG, the dielectric constant of the dielectric layers always influences the boundary effect and the performance of the MTNG. Theoretically, increase of the dielectric constant will lead to the aggregation of electric field lines in the dielectric layers and the decrease of boundary effect, which helps to increase the total output charge density of MTNG. Here, we present a simulated result of the driving channels' charge densities of the MTNG-30 with the dielectric constant ranging from 1.5 to 6 (shown in Fig. S15). When the dielectric constant increases, the charge densities of the channels also increase. Therefore, replacing the dielectric layer with materials with higher dielectric constant is another way to decrease the boundary effect and increase the total output charge density of the MTNG.

Based on the above discussion, we aim at decreasing the boundary effect by decreasing the thickness of the dielectric layer. Experimentally, we fabricated a series of MTNG-30 with dielectric layers' thicknesses of  $30 \mu\text{m}$  and  $21 \mu\text{m}$  and compare the performance with the MTNG-30 with  $60 \mu\text{m}$  thick dielectric layer used before. As Fig. 4d, Fig. S13, Fig. S16 and Fig. S17 show, with the decrease of the dielectric layers thickness, the total output charge density of the MTNG increases. For the MTNG-30 with  $21 \mu\text{m}$  thick dielectric layer, the output charge density is increased to  $5.35 \text{ mC m}^{-2}$ , which is the highest output charge density of TENGs by now (Table S1 shows the output charge densities of reported high output TENGs) and this value could be further increased through adding more driving channels, using thinner dielectric layers or dielectric layers with higher dielectric constant.

#### 2.4. MTNG's ability to avoid crosstalk noise

Usually, if we use a single general electrical source such as N-TENG to power multiple devices, these devices are easy to work with large errors, low working efficiency and even damage since the branch voltage or current will change with all devices. Excitingly, MTNG shows its excellent ability to avoid the crosstalk noise and supply stable voltage

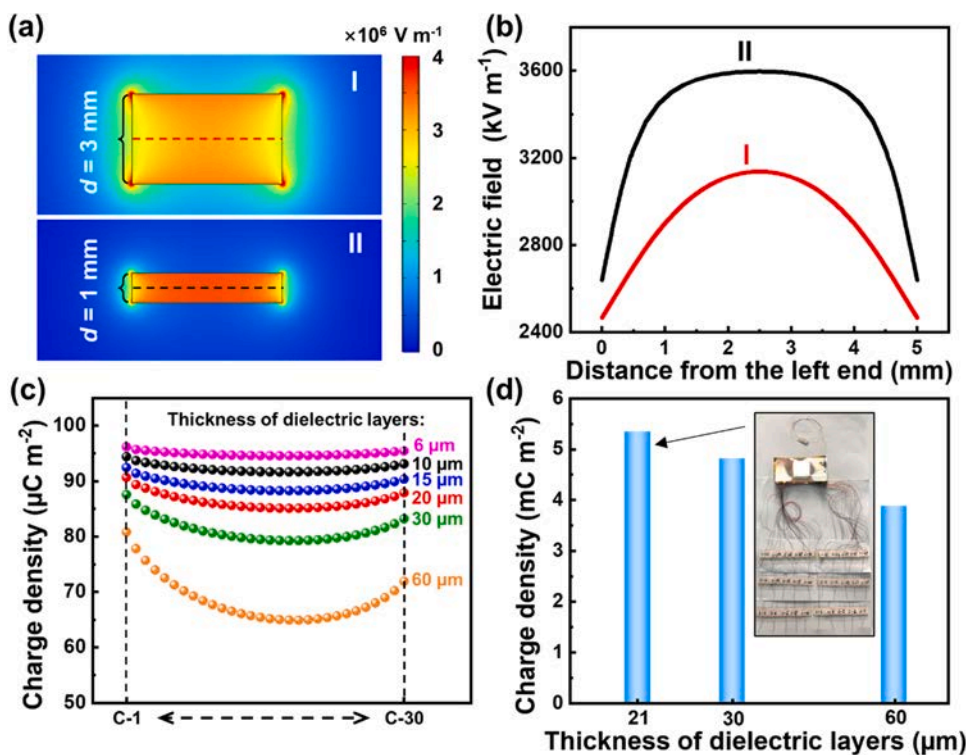


Fig. 4. Increase of the performance of MTNG through decrease the thickness of dielectric layers. (a) Simulated result of the electric field intensity distribution generated by two charged layers with different separation distance  $d$ . (b) The electric field intensity distribution along the lines marked by the dotted line in Fig. 4a with different distance from the left end. (c) Simulated result of the charge densities MTNG-30's driving channels with the thickness of the dielectric layers ranging from 6 to  $60 \mu\text{m}$ . (d) A bar graph shows the relationship of the output charge densities ranges with the thickness of dielectric layers, the insert shows optical image of the MTNG-30 with  $21 \mu\text{m}$  dielectric layers.

and current for each device simultaneously and independently. Fig. 5a shows the schematic of how to use MTNG to power multiple devices, in which each device is powered by one driving channel of MTNG. Using the circuits shown in Fig. S18 and Fig. 5a, 10 light sensors are simultaneously driven by a N-TENG or a MTNG-10. In the experiment, 10 sensors are divided into two groups containing 5 sensors each, one group (Group-1) keeps working under white light illumination of 420 lux, and the other group (Group-2) working in dark or disconnected. Output signals of the sensors are tested, and the output signals of Group-1 corresponding to Group-2 working in different states are compared to evaluate the crosstalk among the sensors. As Fig. 5b (the output signals of sensor-3 (one sensor of Group-1)) and Video S1 show, using the N-TENG as power source, when the state of Group-2 changes from light to dark and disconnected, though sensor-3 works in a stable light, its output signal ranges from about 1.4–2.0  $\mu\text{A}$  and 3.1  $\mu\text{A}$ , which caused by crosstalk among the sensors. Relatively, using the MTNG-10 as power source, when the state of Group-2 changes in the same manner, the output signal of sensor-3 is almost stable (change < 2%). At the same time, as Fig. S19 shows, the output signals of all sensors of Group-1 show similar characteristic with Sensor-3. That is to say, using the MTNG-10 as power source, output signals of the sensors are not influenced by the other sensors, and the crosstalk noise is effectively avoided.

### 2.5. Increment of the working efficiency of MTNG driven devices

Except for the ability to avoid the crosstalk noise as a multi-channel power source, MTNG could also increase the working efficiency in some applications, as the output charge density of the MTNG is increased to a very high value. As Fig. S20 and Video S2 show, an MTNG-10 is used to power 10 electrochemical deposition equipments, and the N-TENG is used to power one equipment as the control group. Output currents of the MTNG and the N-TENG are rectified to direct current before powering the electrochemical deposition equipment (the rectified currents are shown in Fig. S21a). As shown in the optical images and atomic force microscope (AFM) images of Fig. 5c, after 1 h deposition, 10  $\text{MnO}_2$  patterns were deposited on the patterned ITO electrodes simultaneously

powered by the MTNG-10. According to the line thickness tracks in AFM images (Fig. S21b), the average thicknesses of the patterns are calculated (Fig. 5d). It is clear that, though the thicknesses of one pattern deposited with MTNG-10 are a little thinner than that deposited with N-TENG, the total thickness of ten patterns is about 3.6 times that of deposited with the N-TENG, which means MTNG greatly improves the electrochemical deposition efficiency.

### 2.6. Driven of high-power devices with MTNG

Furthermore, output energy of the MTNG could be collected together to power one device which needs high power. Using the circuit shown in Fig. 6a and b, output energy of the N-TENG and the MTNG are stored in capacitors and then used to power a digital watch. Through controlling the switchers, the capacitors alternate between the charging state and the discharging state. As Fig. 6c and Video S3 show, the capacitors are first charged for 7 mins, and the stored energy is used to power the watch. As a result, the watch could work for 4 mins and 15 s using the N-TENG, it is shorter than the charging time, which means that the watch could not be powered continuously with the N-TENG. However, the working time of the watch is increased to 13 mins and 15 s using the MTNG, which is about twice of the charging time and 3.1 times of the working time charged with the N-TENG, and the watch could be powered with the MTNG continuously. This result indicates that MTNG is capable of powering device with rather high energy consuming.

## 3. Conclusions

In summary, we designed and developed a MTNG utilizing  $E_{\text{ext}}$  to greatly increase the output charge density of TENGs. Through constructing the restricted  $E_{\text{ext}}$  and designing a series of driving channels inside, the multiple channels can work simultaneously driven by one friction layers pair. The output current and charge density of each channel is close to that of the N-TENG, and the total output charge density is increased to many times that of the N-TENG consequently. Moreover, increasing the number of driving channels, using thinner

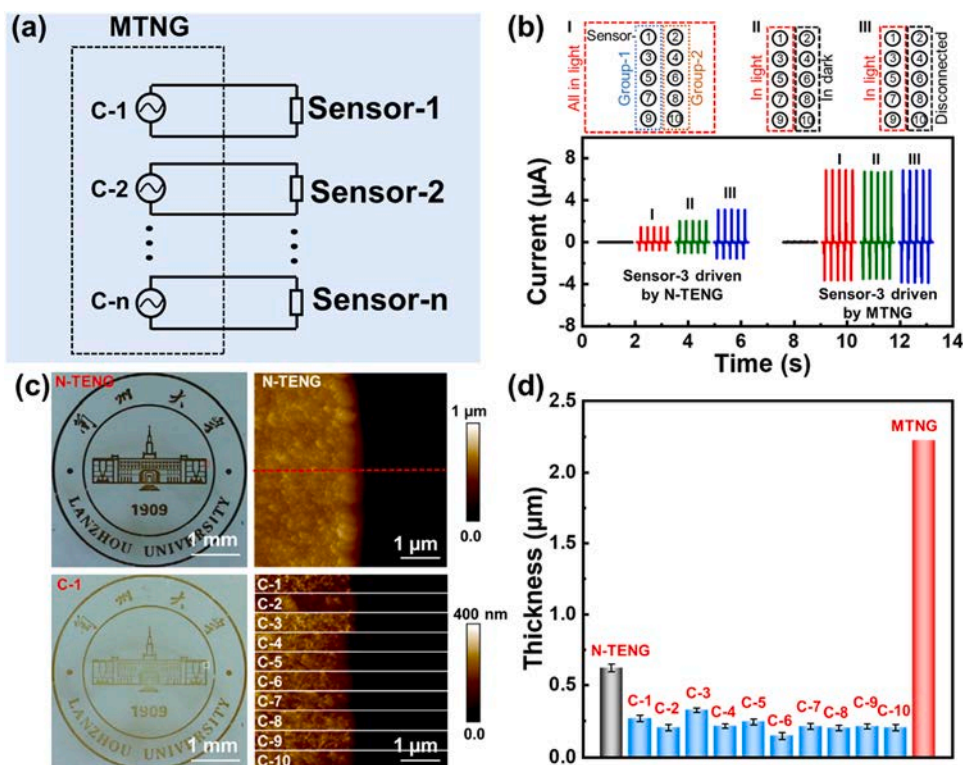


**Fig. 5.** MTNG's ability to avoid the crosstalk noise and to increase working efficiency of devices. (a) Schematic diagram shows the circuit to power multiple devices with the MTNG. (b) Comparison of the output signals of sensor-3 when driving 10 light sensors simultaneously by a N-TENG or a MTNG-10, the sensors are divided into two groups (as shown in (I) and working with all sensors in white light (420 lux) (I) or with Group-1 work in light and Group-2 work in dark (II) or Group-1 work in light and Group-2 is disconnected (III). The black lines show the output signals of sensor-3 when all sensors in dark. Output signals of all 10 sensors are shown in Fig. S19. (c) Optical images and AFM images of the  $\text{MnO}_2$  patterns deposited by the N-TENG and the driving channels of the MTNG-10, the red squares in the optical images show the places to obtain the AFM images. (d) Statistic results of the thickness of the deposited patterns.

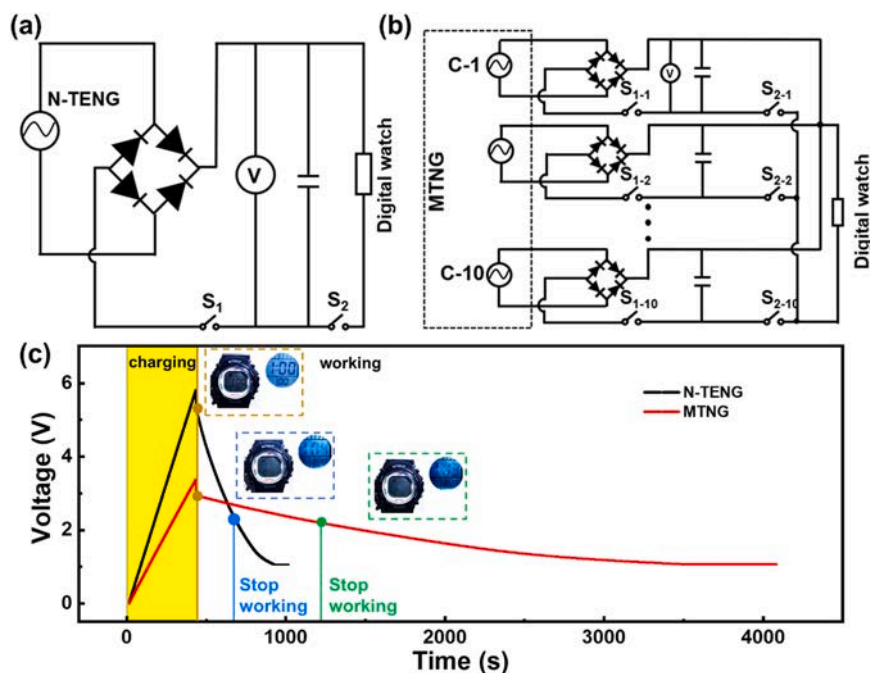


**Fig. 6.** A digital watch powered by the N-TENG and the MTNG-10. (a) Schematic illustrations of the circuit to power the digital watch using the N-TENG. (b) Schematic illustrations of the circuit to power the digital watch using the MTNG-10. (c) Voltages the capacitors in the circuits in the charging and discharging process, and the insets show the optical images of the watch at the start and stop working time.

dielectric layers or dielectric layers with higher dielectric constant are proved effective to further increase the output charge density. In this work, the output charge density of MTNG is increased up to 20 times that of a N-TENG with a new output record of  $5.35 \text{ mC m}^{-2}$  being obtained. In addition, as a power source with multiple output channels, MTNG shows the unique ability as a stable multi-channel power source to avoid crosstalk noise between driving devices. Comparing with multiple devices driven by the N-TENG, their working efficiency are also increased when they are driven by the MTNG. By storing the output energy in capacitors, MTNG could be used to power device with higher energy consuming.

## 4. Material and methods

### 4.1. Preparation of the PVDF solution and PA solution [37]

3.75 g PVDF powder is dissolved in 8.5 g N,N-dimethylacetamide and 12.75 g acetone, stirred for 30 mins at  $60^\circ\text{C}$  and then cooled down to room temperature to prepare the PVDF solution. 2 g PA powder is dissolved in 4.8 g formic acid and 3.2 g dichloromethane and then it is stirred for 1 h to make all PA powders dissolved to prepare the PA solution.

### 4.2. Preparation of PVDF and PA nanofibers [37]

PVDF and PA nanofibers are prepared via electrospinning. In the experiment, an aluminum foil is used as the collector and the prepared PVDF or PA solution is loaded into a syringe. The distance between the needle of the syringe and the collector is set to 16 cm. To prepare the PVDF nanofibers, feed rate of the PVDF solution is set to  $3 \text{ mL h}^{-1}$ , and the voltage between the needle and the collector is set to 15 kV. To prepare the PA nanofibers, feed rate of the PVDF solution is set to  $1 \text{ mL h}^{-1}$ , and the voltage between the needle and the collector is set to 16 kV. The nanofibers are collected for 10 mins and then dried at  $60^\circ\text{C}$  for 30 mins.

### 4.3. Fabrication of the N-TENG

First, two piece of cleaning PET films ( $4 \text{ cm} \times 4 \text{ cm}$ ,  $30 \mu\text{m}$  thick) with Cr/Ag electrodes ( $3 \text{ cm} \times 3 \text{ cm}$ ) deposited on one side are prepared. On the other side, PVDF or PA nanofibers is adhered on the surface with following steps: the electrospinning nanofibers is first peeled off from the aluminum foil and cut into square of  $3 \text{ cm} \times 3 \text{ cm}$ . On the surface of the PET film, a piece of very thin double side tape is pasted at the needed location, and then the nanofibers are pasted on the double side tape. Eventually, copper wires were connected to the Cr/Ag electrodes, and the films are assembled as that shown in Fig. S8 to make the N-TENG.

### 4.4. Fabrication of the MTNG

First, two piece of cleaning PET films ( $4 \text{ cm} \times 4 \text{ cm}$ ,  $30 \mu\text{m}$  thick) with Cr/Ag electrodes ( $3 \text{ cm} \times 3 \text{ cm}$ ) deposited on one side are prepared and copper wires were connected to the electrodes. On the other side of PET films, PVDF or PA nanofibers is adhered on the surface. The electrode at the back of the PA film acts as one electrode of the driving channels and the electrode at the back of PVDF film act as one restriction electrode. Second, several pieces of cleaning PI films ( $4 \text{ cm} \times 4 \text{ cm}$ , thickness of the films depends on the needed thickness of the dielectric layers in the driving channels) with Cr/Ag electrodes ( $3 \text{ cm} \times 3 \text{ cm}$ ) deposited on one side are prepared and copper wires were connected to the Cr/Ag electrodes. The PI films are pasted layer by layer on the back side of the PET film with PA nanofibers to make the driving channels, and the PI film and the glue formed the dielectric layer in the driving channels. At the top of the driving channels, another film is pasted as another restriction electrode. Eventually, the restriction electrodes are connected with a copper wire, and films are assembled as that shown in Fig. 1c to make the MTNG.

### 4.5. Measurement of the MTNG

In the actual measurement, restricted to the measurement equipment we used. Outputs of each driving channel are measured in order, with all

channels at the same state (all channels short-circuit connected to measure the output current, all channels connected with a load resistance same with the measurement equipment (100 M $\Omega$ ) to measure the output voltage). The MTNG is driven by a linear motor with an amplitude of 2 cm and a frequency of 4 Hz.

#### 4.6. Calculation of the energy stored in the capacitors

The energy stored in the capacitors are calculated by the equation:  $E = CV^2/2$ . Here,  $E$  is the energy stored in the capacitor,  $C$  is the capacitance of the capacitor and  $V$  is the voltage of the charged capacitor.

#### 4.7. Measurement of the light sensors driven simultaneously by a N-TENG or a MTNG-10

As Fig. S18 shows, to drive the 10 sensors simultaneously by a N-TENG, all sensors are connected in parallel, and then connected to the N-TENG; to drive the 10 sensors simultaneously by a MTNG, each sensor is connected directly to one driving channel of the MTNG-10.

The sensors are divided into two groups: Group-1 contains Sensor-1, Sensor-3, Sensor-5, Sensor-7 and Sensor-9, Group-2 contains Sensor-2, Sensor-4, Sensor-6, Sensor-8 and Sensor-10. First, dark currents of the sensors are measured through place all the sensors in dark. Then the sensors are measured in the following states: (I) all sensors work in light; (II) Group-1 work in light and Group-2 work in dark; (III) Group-1 work in light and Group-2 is disconnected. In the experiment, 420 lux white light is used to illuminate the sensors.

#### 4.8. Powering electrochemical deposition devices with the N-TENG and the MTNG-10

First, an electrochemical deposition solution was prepared by adding 0.358 g Mn(NO<sub>3</sub>)<sub>2</sub> aqueous solution (50 wt%) and 0.425 g NaNO<sub>3</sub> to 50 mL of deionized water and stirring continuously for 30 min at room temperature [38]. Second, patterned ITO glass and carbon electrode are immersed in the solution as the working electrodes. The electrodes and the solution formed the electrochemical deposition devices. Third, as Fig. S20 shows, the N-TENG or each driving channel of the MTNG-10 is connected to the input ends of a rectifier bridge, and the output ends are connected to an electrochemical deposition device with the positive end connected with the carbon electrode and the negative end connected with the patterned ITO glass. Then the N-TENG or the MTNG is driving with a linear motor for 1 h. After that, the ITO glasses are washed with deionized water for several times to remove the excess electrolyte and dried at 60 °C for 1 h.

#### 4.9. Measurement of thickness of the deposited patterns

The deposited patterns are first imaged by AFM at the position marked by the red square shown in Fig. 5c, and line thickness tracks (as that shown in Fig. S21b) are then obtained from the AFM images, thicknesses of the deposited patterns are calculated by the line thickness tracks.

#### CRediT authorship contribution statement

Y.Q., L.C. and R.C.Z. raise the idea and designed the MTNG, R.C.Z., L.C., M.M.H., S.B., P.Z. S., X.F.J., and W.H.G. fabricated and measured the device, R.C.Z., L.C., Q.X. and J.W. conducted the simulation via COMSOL, R.C.Z., L.C. and Y.Q. analyzed the experimental data, plotted the figures and prepared the manuscript, and all authors reviewed and commented on the manuscript.

#### Declaration of Competing Interest

The authors declare that they have no known competing financial interests or personal relationships that could have appeared to influence the work reported in this paper.

#### Acknowledgments

This work was supported by the National Key Research and Development Project (2021YFA1201602), the National Natural Science Foundation of China (No. U21A20175, 52172203).

#### Appendix A. Supporting information

Supplementary data associated with this article can be found in the online version at doi:10.1016/j.nanoen.2022.107272.

#### References

- [1] N. Zhang, C. Qin, T.X. Feng, J. Li, Z.R. Yang, X.P. Sun, E.J. Liang, Y.C. Mao, X. D. Wang, Non-contact cylindrical rotating triboelectric nanogenerator for harvesting kinetic energy from hydraulics, *Nano Res.* 13 (2020) 1903–1907.
- [2] W.H. Xu, H.X. Zheng, Y. Liu, X.F. Zhou, C. Zhang, Y.X. Song, X. Deng, M. Leung, Z. B. Yang, R.X. Xu, Z.L. Wang, X.C. Zeng, Z.K. Wang, A droplet-based electricity generator with high instantaneous power density, *Nature* 578 (2020) 392–396.
- [3] J. Chen, Y. Huang, N.N. Zhang, H.Y. Zou, R.Y. Liu, C.Y. Tao, X. Fan, Z.L. Wang, Micro-cable structured textile for simultaneously harvesting solar and mechanical energy, *Nat. Energy* 1 (2016) 16138.
- [4] R. Hinchet, H.J. Yoon, H. Ryu, M.K. Kim, E.K. Choi, D.S. Kim, S.W. Kim, Transcutaneous ultrasound energy harvesting using capacitive triboelectric technology, *Science* 365 (2019) 491–494.
- [5] Z. Liu, H. Li, B.J. Shi, Y.B. Fan, Z.L. Wang, Z. Li, Wearable and implantable triboelectric nanogenerators, *Adv. Funct. Mater.* 29 (2019), 1808820.
- [6] C.X. Lu, J. Chen, T. Jiang, G.Q. Gu, W. Tang, Z.L. Wang, A stretchable, flexible triboelectric nanogenerator for self-powered real-time motion monitoring. *Adv. Mater. Technol.* 3 (2018), 1800021.
- [7] T. Shinbrot, T.S. Komatsu, Q. Zhao, Spontaneous tribocharging of similar materials, *Europhys. Lett.* 83 (2008), 24004.
- [8] S.H. Wang, J. Xu, W.C. Wang, G.J.N. Wang, R. Rastak, F. Molina-Lopez, J. W. Chung, S.M. Niu, V.R. Feig, J. Lopez, T. Lei, S.K. Kwon, Y. Kim, A.M. Foudeh, A. Ehrlich, A. Gasperini, Y. Yun, B. Murmann, J.B.H. Tok, Z.A. Bao, Skin electronics from scalable fabrication of an intrinsically stretchable transistor array, *Nature* 555 (2018) 83–88.
- [9] Y. Lee, S.H. Cha, Y.W. Kim, D. Choi, J.Y. Sun, Transparent and attachable ionic communicators based on self-cleanable triboelectric nanogenerators, *Nat. Commun.* 9 (2018) 1804.
- [10] H.Y. Guo, X.J. Pu, J. Chen, Y. Meng, M.H. Yeh, G.L. Liu, Q. Tang, B.D. Chen, D. Liu, S. Qi, C.S. Wu, C.G. Hu, J. Wang, Z.L. Wang, A highly sensitive, self-powered triboelectric auditory sensor for social robotics and hearing aids, *Sci. Robot* 3 (2018), eaat2516.
- [11] H. Hong, X. Yang, H. Cui, D. Zheng, H. Wen, H. Wen, R. Huang, L. Liu, J. Duan, Q. Tang, Self-powered seesaw structured spherical buoys based on a hybrid triboelectric-electromagnetic nanogenerator for sea surface wireless positioning, *Energy Environ. Sci.* 15 (2022) 621–632.
- [12] X. Yang, G. Liu, Q. Guo, H. Wen, R. Huang, X. Meng, J. Duan, Q. Tang, Triboelectric sensor array for internet of things based smart traffic monitoring and management system, *Nano Energy* 92 (2022), 106757.
- [13] F.R. Fan, Z.Q. Tian, Z.L. Wang, Flexible triboelectric generator, *Nano Energy* 1 (2012) 328–334.
- [14] L. Xu, H. Wu, G. Yao, L.B. Chen, X.D. Yang, B.D. Chen, X. Huang, W. Zhong, X. Y. Chen, Z.P. Yin, Z.L. Wang, Giant voltage enhancement via triboelectric charge supplement channel for self-powered electroadhesion, *ACS Nano* 12 (2018) 10262–10271.
- [15] J.H. Nie, X.Y. Chen, Z.L. Wang, Electrically responsive materials and devices directly driven by the high voltage of triboelectric nanogenerators, *Adv. Funct. Mater.* 29 (2019), 1806351.
- [16] R. Lei, Y. Shi, Y. Ding, J. Nie, S. Li, F. Wang, H. Zhai, X. Chen, Z.L. Wang, Sustainable high-voltage source based on triboelectric nanogenerator with a charge accumulation strategy, *Energy Environ. Sci.* 13 (2020) 2178–2190.
- [17] G. Qiao, J. Wang, X. Yu, R. Jia, T. Cheng, Z.L. Wang, A bidirectional direct current triboelectric nanogenerator with the mechanical rectifier, *Nano Energy* 79 (2021), 105408.
- [18] Z. Wang, L. Cheng, Y.B. Zheng, Y. Qin, Z.L. Wang, Enhancing the performance of triboelectric nanogenerator through prior-charge injection and its application on self-powered anticorrosion, *Nano Energy* 10 (2014) 37–43.
- [19] J. Wang, C.S. Wu, Y.J. Dai, Z.H. Zhao, A. Wang, T.J. Zhang, Z.L. Wang, Achieving ultrahigh triboelectric charge density for efficient energy harvesting, *Nat. Commun.* 8 (2017) 88.
- [20] Y. Jiang, K. Dong, X. Li, J. An, D. Wu, X. Peng, J. Yi, C. Ning, R. Cheng, P. Yu, Z. L. Wang, Stretchable, washable, and ultrathin triboelectric nanogenerators as skin-

- like highly sensitive self-powered haptic sensors, *Adv. Funct. Mater.* 31 (2020), 2005584.
- [21] S.H. Wang, Y.N. Xie, S.M. Niu, L. Lin, C. Liu, Y.S. Zhou, Z.L. Wang, Maximum surface charge density for triboelectric nanogenerators achieved by ionized-air injection: methodology and theoretical understanding, *Adv. Mater.* 26 (2014) 6720–6728.
- [22] K. Han, J. Luo, Y. Feng, L. Xu, W. Tang, Z.L. Wang, Self-powered electrocatalytic ammonia synthesis directly from air as driven by dual triboelectric nanogenerators, *Energy Environ. Sci.* 13 (2020) 2450–2458.
- [23] S. Li, Y. Fan, H. Chen, J. Nie, Y. Liang, X. Tao, J. Zhang, X. Chen, E. Fu, Z.L. Wang, Manipulating the triboelectric surface charge density of polymers by low-energy helium ion irradiation/implantation, *Energy Environ. Sci.* 13 (2020) 896–907.
- [24] F.R. Fan, L. Lin, G. Zhu, W.Z. Wu, R. Zhang, Z.L. Wang, Transparent triboelectric nanogenerators and self-powered pressure sensors based on micropatterned plastic films, *Nano Lett.* 12 (2012) 3109–3114.
- [25] J.J. Shao, W. Tang, T. Jiang, X.Y. Chen, L. Xu, B.D. Chen, T. Zhou, C.R. Deng, Z. L. Wang, A multi-dielectric-layered triboelectric nanogenerator as energized by corona discharge, *Nanoscale* 9 (2017) 9668–9675.
- [26] H. Guo, J. Chen, L. Wang, A.C. Wang, Y. Li, C. An, J.-H. He, C. Hu, V.K.S. Hsiao, Z. L. Wang, A highly efficient triboelectric negative air ion generator, *Nat. Sustain.* 4 (2020) 147–153.
- [27] N.Y. Cui, C.H. Dai, J.M. Liu, L. Gu, R. Ge, T. Du, Z. Wang, Y. Qin, Increasing the output charge quantity of triboelectric nanogenerators via frequency multiplication with a multigap-structured friction layer, *Energy Environ. Sci.* 13 (2020) 2069–2076.
- [28] H. Qin, G. Cheng, Y. Zi, G. Gu, B. Zhang, W. Shang, F. Yang, J. Yang, Z. Du, Z. L. Wang, High energy storage efficiency triboelectric nanogenerators with unidirectional switches and passive power management circuits, *Adv. Funct. Mater.* 28 (2018), 1805216.
- [29] X. Cheng, W. Tang, Y. Song, H. Chen, H. Zhang, Z.L. Wang, Power management and effective energy storage of pulsed output from triboelectric nanogenerator, *Nano Energy* 61 (2019) 517–532.
- [30] J. Yang, F. Yang, L. Zhao, W. Shang, H. Qin, S. Wang, X. Jiang, G. Cheng, Z. Du, Managing and optimizing the output performances of a triboelectric nanogenerator by a self-powered electrostatic vibrator switch, *Nano Energy* 46 (2018) 220–228.
- [31] L. Cheng, Q. Xu, Y. Zheng, X. Jia, Y. Qin, A self-improving triboelectric nanogenerator with improved charge density and increased charge accumulation speed, *Nat. Commun.* 9 (2018), 37773.
- [32] Y. Li, M. Bouza, C. Wu, H. Guo, D. Huang, G. Doron, J.S. Temenoff, A.A. Stecenko, Z.L. Wang, F.M. Fernandez, Sub-nanoliter metabolomics via mass spectrometry to characterize volume-limited samples, *Nat. Commun.* 11 (2020) 5625.
- [33] G. Zhu, J. Chen, T. Zhang, Q. Jing, Z.L. Wang, Radial-arrayed rotary electrification for high performance triboelectric generator, *Nat. Commun.* 5 (2014) 3426.
- [34] Y. Liu, W. Liu, Z. Wang, W. He, Q. Tang, Y. Xi, X. Wang, H. Guo, C. Hu, Quantifying contact status and the air-breakdown model of charge-excitation triboelectric nanogenerators to maximize charge density, *Nat. Commun.* 11 (2020) 1599.
- [35] R.P. Feynman, R.B. Leighton, M. Sands, *The Feynman Lectures on Physics*, Addison-Wesley Publishing Company, 1964 (Reference to a chapter in an edited book).
- [36] Y.L. Zi, S.M. Niu, J. Wang, Z. Wen, W. Tang, Z.L. Wang, Standards and figure-of-merits for quantifying the performance of triboelectric nanogenerators, *Nat. Commun.* 6 (2015) 8376.
- [37] Y.B. Zheng, L. Cheng, M. Yuan, Z. Wang, L. Zhang, Y. Qin, T. Jing, An electrospun nanowire-based triboelectric nanogenerator and its application in a fully self-powered UV detector, *Nanoscale* 6 (2014) 7842.
- [38] J. Du, Y. Zhao, Z. Zhang, X. Mu, X. Jiang, B. Huang, Y. Zhang, S. Zhang, Z. Zhang, E. Xie, High-performance pseudocapacitive microsupercapacitors with three-dimensional current collector of vertical ITO nanowire arrays, *J. Mater. Chem. A* 7 (2019) 6220.